JOINT INSTITUTE FOR NUCLEAR RESEARCH

FINAL REPORT ON THE INTEREST PROGRAMME

“Study of radiation effects on advanced materials exposed to electron beams and gamma rays using Raman Spectroscopy”

Supervisor:
Dr. Antonio Leyva Fabelo

Student:
Crismery Coral Rodríguez Bautista
Pedro Henriquez Ureña National University
Santo Domingo, Dominican Republic

Participation period:
March 02 - April 19
Wave 14

Dubna, 2026

Abstract

This research focuses on a comparative analysis of the structural behavior of multi-walled carbon nanotubes (MWCNTs) after being exposed to two types of irradiation sources: gamma radiation and electron radiation. Using Raman spectroscopy as the primary tool, the study aims to determine whether these types of radiation act as degrading agents or, conversely, promote the purification and reordering of the material. To this end, a spectral deconvolution methodology (using the Voigt function) is applied, which allows for the identification of critical bands such as the D'' band and the “low-frequency shoulder,” which are fundamental for evaluating defect density and graphitic quality.

Introduction

Raman spectroscopy has established itself as one of the most powerful non-destructive characterization tools in materials science, due to its ability to provide detailed information on the molecular structure and vibrational modes of carbon-based systems [1]. Based on the inelastic scattering of light, this technique allows for the precise identification of atomic hybridization, the degree of crystalline order, and the presence of defects in the atomic lattice. In the field of nanomaterials, its sensitivity makes it indispensable for the study of multi-walled carbon nanotubes (MWCNTs), where interactions between concentric layers and the integrity of the hexagonal graphene lattice define their physicochemical properties.

The scientific importance of studying MWCNTs under radiation conditions lies in the need to understand how these nanostructures respond to extreme environments. The interaction of nanotubes with gamma radiation and high-energy electron bombardment can induce phenomena ranging from the creation of point defects to the reorganization of chemical bonds, which drastically alter their performance. Analyzing these changes not only expands fundamental knowledge about the resilience of nanomaterials but also allows for the exploration of controlled modification mechanisms to optimize their reactivity or conductivity.

The main objective of this study is to analyze and compare the behavior of a sample of MWCNTs, after being exposed to two types of irradiation sources: gamma radiation and electron radiation. Through a comparative analysis, the study aims to determine the structural changes, the dimensional stability of the lattice, and the evolution of defect density in each case. To achieve an accurate interpretation, the study focuses on the identification of spectral peaks and the application of spectral deconvolution using mathematical functions, which allows for the separation of overlapping signals and the acquisition of quantitative data.

The findings of this research are useful for technological applications in the aerospace industry, radiological medicine, and nuclear engineering, where MWCNT-based devices must operate under constant radiation fluxes. The ability to predict whether radiation acts as a degrading agent or as a method of purification and structural enhancement allows for the design of more resistant and efficient materials.

Material and Methods

Raman spectroscopy

Raman spectroscopy is a scattering technique. It is based on the Raman effect, that is, on the fact that the frequency of a small fraction of the scattered radiation differs from the frequency of the incident monochromatic radiation. It is based on the inelastic scattering of incident radiation through its interaction with vibrating molecules. It analyzes molecular vibrations.

Only a small fraction of scattered radiation has a frequency different from that of the incident radiation and constitutes Raman scattering. When the frequency of the incident radiation is higher than that of the scattered radiation, Stokes lines appear in the Raman spectrum. However, when the frequency of the incident radiation is lower than that of the scattered radiation, anti-Stokes lines appear in the Raman spectrum. Scattered radiation is usually measured at a right angle to the incident radiation

Stokes-shifted Raman bands involve transitions from lower to higher energy vibrational levels; therefore, Stokes bands are more intense than anti-Stokes bands and are thus measured in conventional Raman spectroscopy [1]. It also helps us detect molecular vibrations in the 100–400 cm^{-1} range, a region where many vibrations of inorganic

compounds appear, since this range is not accessible to mid-infrared FTIR spectrometers, and the sample is typically excited using lasers with energies between 1.17 and 2.6 eV (1064 and 477 nm, respectively) [2] [3].

The light source used is a laser beam, which is characterized by being monochromatic (having a single frequency or color) directional, and having the same phase, making it a coherent emission. This allows a high concentration of energy to be focused onto a relatively small area [4].

A standard Raman system operates through the interaction of an excitation source, an illumination system, a wavelength selector, and a detector, as shown in *Figure 1*. To optimize the spectral response, the device features three interchangeable light sources, allowing the user to select the one that produces the best signal. The light is transmitted via optical fiber to strike the sample, and after scattering, the resulting signal is sent to the detector. There, a spectrograph breaks down the light so that a CCD (Charge-Coupled Device) sensor can immediately capture the full spectrum [5].

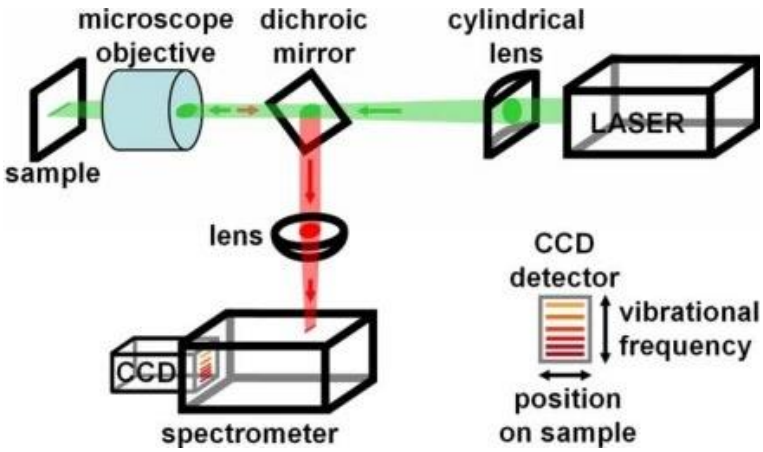

Figure 1. Basic operating diagram of Raman spectroscopy.

The process begins with a transient virtual state which, upon decaying, places the electron in a real energy level while the photon is emitted. This interaction is classified as elastic (or Rayleigh) scattering if the resulting photon retains the energy of the incident photon and the electron returns to its original state. Conversely, if an energy change occurs, the scattering is inelastic. In the latter case, if the photon loses energy, it is called Stokes scattering, while if it gains energy, it is known as anti-Stokes scattering (*Figure 2*).

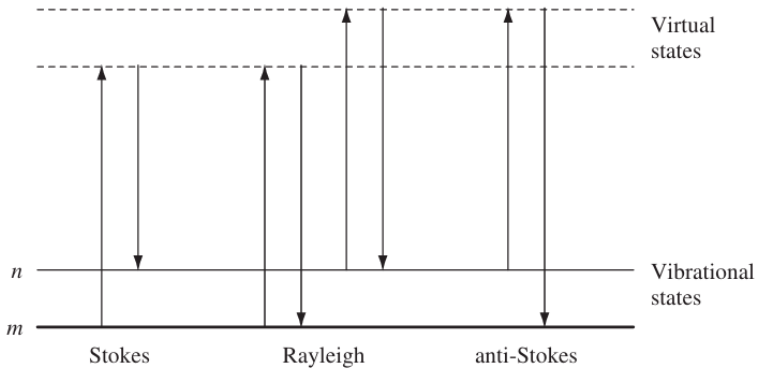

Figure 2. Transient energy states, Stokes, Rayleigh and anti-Stokes.

Raman spectroscopy directly measures the intensity of radiation as a function of frequency (or wavenumber), providing us with unique and useful information regarding various types of nanostructures. Researchers often use this method to identify the properties of carbon nanostructures, such as their purity, concentration, and defects. It is a non-destructive technique for the detailed determination of the structural characteristics of single-walled carbon nanotubes [6].

Other spectroscopic techniques, such as IR and Raman spectroscopy, provide information about the molecular symmetry of relatively small molecules and the functional groups in long, complex molecules [7]

Applications.

Characterization: can characterize the molecular morphology of carbon materials, since each band in their spectrum is directly linked to a specific vibrational frequency of the molecular bonds. This vibrational frequency and the resulting position of the Raman band are highly sensitive to both the orientation of the bonds and the mass of the atoms involved in the bond, allowing for a detailed analysis of the material's structure [8].

Structural Chemistry: It is possible to determine the structures of molecules in an electronically excited state, as well as those unstable species resulting from laser photolysis at low temperatures.

DNA-Drug Interactions: Using Raman resonance (RR) spectroscopy, the mechanism of drug interaction can be clarified, since the drug's vibrations are selectively enhanced by resonance if the drug exhibits strong absorption in the visible region [9].

Biological: Various nanoparticles (metallic, ceramic, and polymeric) possess properties critical to the biological sector, such as magnetism, biocompatibility, and light emission. Using Raman spectroscopy, it is possible to characterize these particles and obtain essential information about their behavior and interaction with the biological environment in which they are applied.

Mineralogy: Raman spectroscopy stands out as an essential methodology due to its non-destructive nature, high precision, and speed of execution; it allows for detailed characterization through point, line, or spatial (2D and 3D) mapping, facilitating the comprehensive study of the composition of gemstones, minerals, and cultural heritage assets, such as works of art and historical objects [10].

There are numerous applications for Raman spectroscopy, a technique that has established itself as an indispensable tool due to its non-destructive nature and high chemical specificity; not only does it allow us to identify components at the molecular level, but it also facilitates the study of complex interactions in various environments, positioning itself as a cornerstone of contemporary scientific research and industrial technological development.

MWCNT

Carbon nanotubes (CNTs) typically occur in nature and in synthetic form as clusters or bundles of varying diameters, where each individual unit may have heterogeneous dimensions in terms of length and diameter. Exhibit the form of cylindrical carbon molecules and unique features that make them extremely useful in a plethora of applications especially in nanotechnology, electronics, optics and many other fields of materials science. A carbon nanotube can be defined as a tube-shaped material, entirely made from carbon, having the diameter measuring on the nanometer scale, and can be as thin as a few nanometers but as long as hundreds of microns [11].

These nanostructures are not perfect, as they exhibit structural imperfections located both at their ends and along their side walls. Among the most common defects is the presence of pentagonal or heptagonal rings, which alter the hexagonal symmetry of

the lattice and generate concave or convex curvatures that deform the nanotube's cylinder. Another significant type of defect is the transition of carbon atoms from sp^2 hybridization to sp^3 hybridization, which disrupts the electronic conjugation of the structure.

Furthermore, chemical purification processes, which typically employ strongly oxidizing conditions, can cause significant damage such as the opening of the nanotube ends. These reactions lead to the formation of carboxyl functional groups at the ends and on the sidewalls, altering the material's surface chemical reactivity. In terms of their physicochemical behavior, carbon nanotubes are characterized by being insoluble in the vast majority of organic solvents.

Despite this limitation, stable dispersions have been successfully obtained in highly polar solvents, such as N,N-dimethylformamide (DMF), N-methylpyrrolidine, and hexamethylphosphoramide (HMPA). This low solubility represents a technological challenge that is typically addressed through functionalization techniques, which allow the modification of the material's properties to facilitate its processing. Chemical functionalization is a versatile tool that enables the incorporation of organic moieties into the nanotube structure to improve its solubility and compatibility with other media.

Thanks to the unique architecture of CNTs, there are various approaches to carrying out these modifications: direct functionalization on pre-existing defects, the creation of covalent bonds on the sidewalls, non-covalent interactions (such as π-π stacking), and endohedral inclusion, which consists of encapsulating molecules or atoms within the internal cavity of the tube [12].

Carbon nanotubes (CNTs), which are commonly incorporated into polymer composites to optimize their conductivity properties, are primarily categorized as single-walled carbon nanotubes (SWCNTs) and MWCNTs. While SWCNTs are structurally defined as individual cylinders composed entirely of carbon atoms, MWCNTs consist of a concentric arrangement comprising an outer tube and at least one inner tube, which are held apart from each other by interatomic forces [11].

Other types of nanotube structures include nanographite, carbon black nanoparticles, and fullerenes, as shown in *Figure 3.*

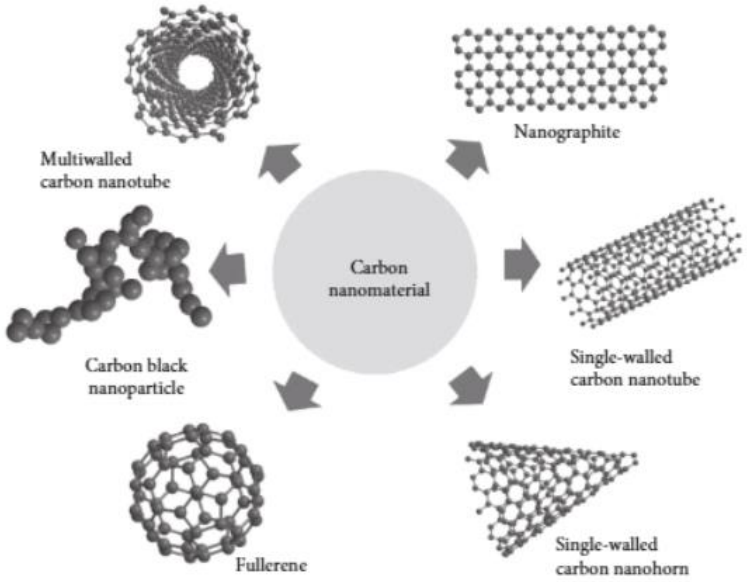

Figure 3. Classification of carbon nanotubes by structure.

Multi-walled carbon nanostructures (MWCNTs) consist of cylindrical sheets of graphene, which are stiffer than currently available carbon fibers; they are produced at the cathode by a direct-current arc discharge between graphite electrodes in an inert gas and methane [13].

MWCNTs are structured as graphene sheets rolled into concentric cylinders with diameters reaching tens of nanometers. Due to these considerable dimensions and the coexistence of tubes with a wide range of diameters, their Raman spectra often lack the distinctive signals that distinguish single-walled carbon nanotubes (SWCNTs) from conventional graphite. For example, although the radial breathing mode (RBM) is detectable in inner tubes smaller than 2 nm under optimal resonance conditions, this signal is generally not visible; this occurs because the response of the wider tubes is extremely weak, and the averaging of the various inner diameters ends up broadening and blurring the signal in the spectrum.

Unlike small-diameter SWCNTs, where the separation between the G+ and G- bands is very pronounced, in the MWCNTs this distinction is weak and tends to blur. This phenomenon is due both to the distribution of diameters within each individual nanotube and to the structural variability present in the experimental samples, resulting in a G band with a slightly asymmetric shape and a peak near the graphite frequency. On the other hand, electron irradiation exerts a significant influence on these materials, causing the appearance of radiation defects that degrade the nanotubes, a process

linked to both the creation of vacancies and the breaking of chemical bonds during treatment [14].

Aplications:

- **Dispersions and coating:** Wear resistant coating for UNCD (ultrananocystalline diamond), CDDSC (Cabide-derived diamond-structured carbon), UDD composites (Ultra-disperd diamond).
- **Optical coatings CNTsC, medical applications.**
- **High surface area materials:** Drug delivery, energy storage, molecular sives.
- **Consolidated materials:** ultrahight-streght structural materials, MEMS components
- **Functional nanostructures:** cold cathodes, transistors, proximal probe tip.

Vibrational Modes Analysis (Raman Spectroscopy)

D Band (Disorder Band): Located around **1350 cm^{-1}**, it is associated with the presence of carbon impurities with sp^3 hybridization. An increase in the intensity of this band indicates the breaking of sp^2 bonds and the formation of new sp^3 bonds, reflecting greater structural disorder.

G Band (Graphitic Band): Observed near **1580 cm^{-1}**, it is characteristic of sp^2 hybridized carbon systems. It originates from the in-plane stretching vibrations of C-C bonds in both aromatic rings and chains. Its Full Width at Half Maximum (FWHM) is a critical indicator of the sample's crystallinity; furthermore, this band is highly sensitive to the structural strain of the material.

2D Band (or G^l): Situated around **2700 cm^{-1}**, this band arises from a second-order, two-phonon scattering process. Unlike the D band, it does not require defects for activation. Its shape and intensity provide essential information regarding the number of layers or walls present in the structure.

D+G Band: Occurring at approximately **2930 cm^{-1},** this is a combination peak involving phonons with different momenta, thus requiring the presence of defects for activation.

Its appearance is clear evidence of a high degree of structural disorder, being especially relevant in the characterization of graphene oxide.

D^{II} - It typically appears around **1500 cm^{-1}**. This band has been reported to be associated with amorphous sp^2-bonded forms of carbon, that is, regions where the graphitic network is disordered but still maintains sp^2 hybridization. Some authors consider it a sub-defective mode related to vibrations in very small or highly disordered graphitic domains. It reflects the presence of amorphous sp^2 phases, such as vitreous carbon or turbostratic regions.

Low frequency shoulder – its origin has not been clearly identified. Probably the shoulder has its origin in double resonance process, because its Raman shift (~1200 cm^{-1}) is a point on phonon dispersion [15].

Table 1. Summary: Raman Bands in MWCNT.

Band	**Position (cm^{-1})**	**Name**	**Structural Meaning**	**Diagnostic Notes**
D	~1350	D band	Disorder-induced mode activated by double resonance. Linked to defects, edges, and finite crystallite size in sp^2 carbon.	Intensity relative to G (I_D/I_G) is widely used to estimate defect density.
G	~1580	G band	Graphitic mode (E_2g symmetry). Represents in-plane stretching of sp^2 C–C bonds.	Sharp and intense in well-ordered CNTs; shifts slightly with strain or doping.
D^{I}	~1620	D prime band	Another defect-related mode, weaker than D.	Often appears as a shoulder near G; its

Band	Position (cm^{-1})	Name	Structural Meaning	Diagnostic Notes
			Associated with intravalley scattering.	presence confirms additional disorder.
D^{II}	~1500	D^II band	Reported in some CNT and carbon fiber spectra. Associated with amorphous sp^2-bonded carbon phases.	Not universal; stronger in samples with higher amorphous carbon content. Serves as a marker of purity.
2D (G^{I})	~2700	2D band (also G′)	Second-order overtone of D, activated without defects. Sensitive to stacking order and number of graphene layers.	In CNTs, shape and intensity vary with diameter, number of walls, and electronic resonance conditions.
Combination bands	2400–3200	D+G, D+D′, etc.	Higher-order modes reflecting complex phonon interactions.	Useful for confirming resonance conditions and distinguishing between CNTs and other carbon allotropes.

Additional Notes

- **D^{II} band** not always present; when observed, it indicates **amorphous sp^2 carbon domains**. Its relative intensity compared to D and G can help distinguish **MWCNTs with high crystalline quality** from those contaminated with amorphous carbon.
- Raman spectra of CNTs are highly dependent on **laser excitation wavelength,** which can enhance or suppress certain bands **(resonance effects).**
- Ratios such as **ID/IG** and the presence/absence of DII are practical tools for evaluating CNT synthesis methods (arc discharge, CVD, laser ablation).

- In single-walled CNTs (SWCNT), radial breathing modes (**RBM**) appear at low frequencies (~100–300 cm^{-1}), but in MWCNTs these are usually absent or very weak.
- In MWCNTs of low crystalline quality or with high amorphous carbon content, the D^{II} band is usually more evident. In well-graphitized MWCNTs, the intensity of D^{II} decreases or even disappears, because the structure approaches ordered graphite. Its presence can serve as an indicator of structural purity, differentiating nanotubes with high amorphous carbon content from those with more crystalline walls.
- The relative intensity of D, G, and D^{II} can be used as an **indicator of the structural purity** of MWCNTs. Comparative analysis of these bands is fundamental for evaluating the quality and degree of order in the nanotubes.
- The **low-frequency shoulder** in MWCNT Raman **spectra is not a defect-related band** like D or D^{I}, but rather a collective vibrational signature of concentric walls. Its study provides insight into diameter, wall coupling, and sample purity, making it a valuable tool for characterizing multi-walled nanotubes.

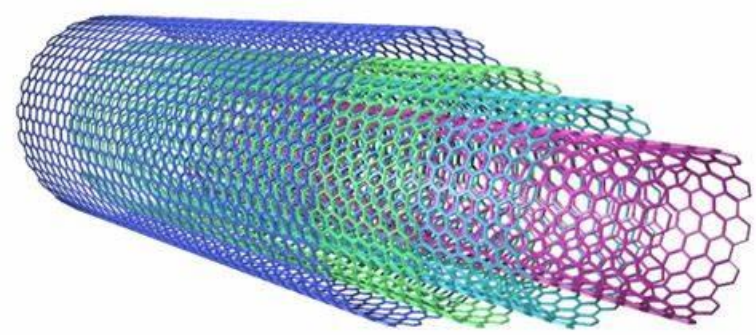

Figure 4. Structure of multi-walled carbon nanotube.

The analized MWCNT powder samples are commercial and 90% pure.

Irradiation facilities

Irradiation with photons of 1.25 MeV (^{60}Co) was performed in a therapeutic gamma chamber РОКУЕМ available at the Medical Complex of the DLNP at the Joint Institute

for Nuclear Research (JINR). The dose power of the chamber is 148.47 Gy/h. The total exposure dose of the irradiated samples was 23.4 kGy.

The photo in *Figure 5* shows the equipment used, and the exposure to radiation was done by rotating the head so that the window was directed upwards, and the samples were placed directly on top of it. The irradiation time was selected so that the samples received the relevant exposure dose.

Figure 5. ^{60}Co radiotherapy chamber similar to the one used in the experiment.

Electron irradiation was performed on the JINR LINAC-800 linear accelerator. Its general scheme is presented in *Figure 6*. The picture in *Figure 7* presents a panoramic view of the accelerator.

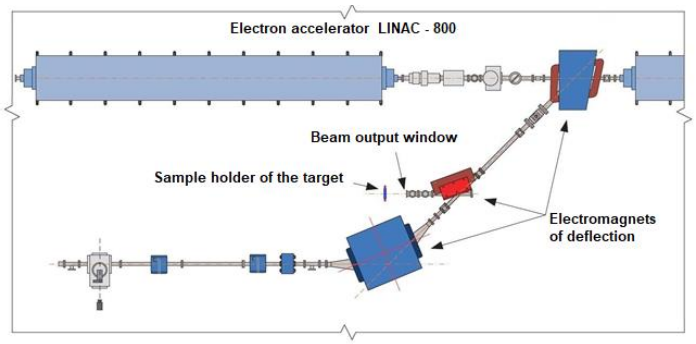

Figure 6. Overview of the LINAC-800 accelerator and the 20 MeV irradiation station.

Figure 7. Panoramic view of the LINAC-800 linear accelerator.

The samples were placed directly in front of the electron output Ti window.

The parameters of the beam are energy 20 MeV, current 10 mA, frequency 10 Hz, and pulse duration 1.5 μs. The fluence in the sample was 4.38×10^{18} e^- cm^{-2}.

Raman spectrometer

The Raman measurements were done at room temperature in backscattering geometry, using a spectrometer model Solar TII (*Figure 8*), applying the following

conditions: diffraction grating of 1200 lines/mm, objective 40x (model Olympus-UPlanFL N), and acquisition time 70 s.

Figure 8. Solar TII Raman spectrometer setup.

Mathematical processing

The post-processing of the spectra was performed using the software package ORIGIN v9. The data obtained from the measurements was normalized and used to plot the spectra. They were plotted on the same graph so the differences that appear after the irradiation can be seen more clearly.

Each spectrum underwent the process of deconvolution, to find every peak and its intensity. The decomposing of peaks was done using the *Peak Analysis* feature of the Origin software.

The post-processing of the spectra was performed using the software package ORIGIN v9. The data obtained from the measurements was normalized and used to plot the spectra. They were plotted on the same graph so the differences that appear after the irradiation can be seen more clearly.

Each spectrum underwent the process of deconvolution to find every peak and its intensity. The decomposing of peaks was performed using the Peak Analysis feature of the Origin software, employing the Voigt function for the fitting process [ ]. This allowed for a more precise characterization of the Raman modes by accounting for both the Gaussian and Lorentzian broadening components of the signals OriginLab Corporation [16].

Interaction of gamma quanta and light particles with matter

Gamma rays are defined as a form of high-energy electromagnetic radiation that originates in the atomic nucleus or through annihilation processes between matter and

antimatter. As photons, they have no mass or electric charge, which allows them to pass through matter via discrete interactions with atoms. During this passage, the photon may be completely absorbed, transferring all its energy to the medium, or it may be scattered, retaining much of its initial energy while changing only its trajectory [17].

On the other hand, light particles (LP), which include electrons (e-), positrons (e+), and beta particles (β), are characterized by their very small mass and electric charge. Unlike gamma rays, electrons interact continuously with the medium through elastic and inelastic collisions. In elastic collisions, the particle undergoes sudden deflections when interacting with nuclei, generating irregular “zigzag” trajectories; this causes its effective range (the penetration depth) to always be less than the total distance traveled within the material.

As for the transfer of energy by electrons, this occurs primarily through inelastic and radiative collisions. In inelastic collisions, the electron transfers its energy to excite or ionize the atoms in the medium, raising atomic electrons to higher energy states or knocking them out of their orbits, which can result in the emission of light.

At the same time, there are radiative collisions, in which the sudden deceleration of an electron as it passes near a heavy nucleus causes the emission of photons—a phenomenon known as bremsstrahlung. Finally, the sources and applications of these types of radiation are varied. While gamma rays originate from nuclear decay, high-energy electrons can be generated artificially in vacuum chambers. An everyday example of electron excitation and ionization occurs in fluorescent light bulbs. Likewise, when electrons accelerated to kilovolt energies strike targets made of heavy elements such as tungsten, the displacement of electrons from inner orbits produces X-rays, a high-energy radiation widely used in medicine and industry [18].

The interaction of photons with matter occurs through five different mechanisms, which are: photoelectric absorption, Compton scattering, pair production, coherent scattering, and photodisintegration.

In these processes, energy is transferred from the photon to the electrons of the tissue or material and is subsequently distributed through multiple Coulomb force

interactions. The first three mechanisms are the most significant, being influenced both by the atomic number of the absorbing medium and by the quantum energy level of the incident photon.

Photoelectric absorption: Also known as the photoelectric effect, this is the most significant interaction of low-energy photons with matter; this effect predominates in the energy range of photons from 0 to 0.5 MeV. Diagram presented in *Figure 9* illustrates the photoelectric effect.

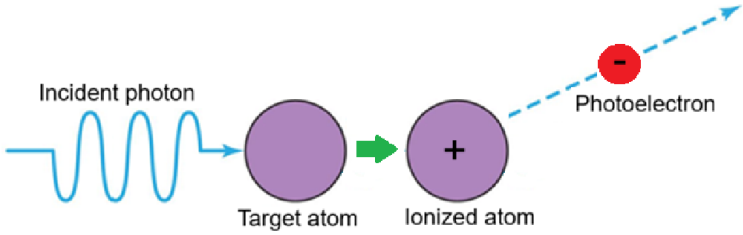

Figure 9. Photoelectric effect.

Compton scattering: The Compton effect, as seen in *Figure 10*, occurs when photons from a gamma-ray beam collide with free electrons or weakly bound electrons, known as target electrons, which behave independently during this incoherent scattering. In this process, the photon transfers part of its energy and momentum to the “initially stationary” electron, causing the photon to scatter with lower energy and a longer wavelength. The fraction of energy lost by the photon is entirely absorbed by the now-called recoil electron in the form of kinetic energy, thereby satisfying the laws of conservation of energy and momentum.

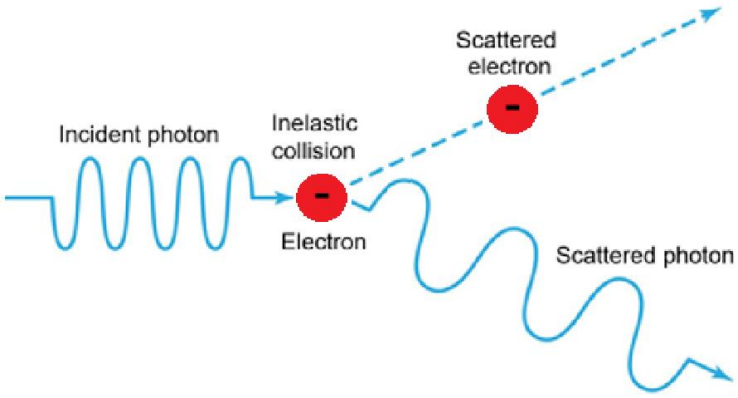

Figure 10. Compton scattering of a photon by an electron.

Pair Production: Also known as energy creation, is the predominant mechanism in high-energy photon interactions and occurs when a γ-ray photon, passing near the electromagnetic field of an atomic nucleus, transforms into an electron-positron pair (*Figure 11*). For this phenomenon to occur, the photon must possess a minimum energy of 1.022 MeV—equivalent to the sum of the rest masses of both particles (0.511 MeV each)—so that any excess energy above this threshold is transferred to the electron and positron in the form of kinetic energy. In this process, the laws of conservation of energy and momentum are strictly obeyed, resulting in the creation of matter from pure electromagnetic radiation when the photon interacts with the intense nuclear field.

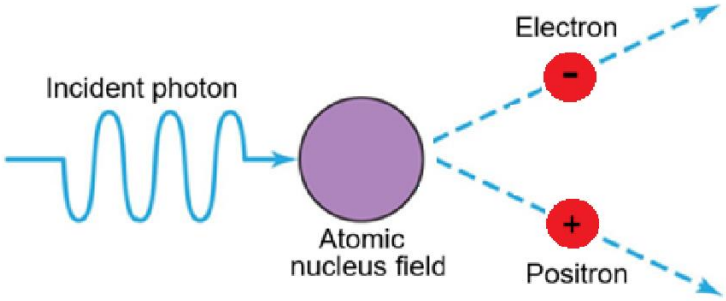

Figure 11. Photon-induced electron–positron pair production.

Coherent Scattering: Also known as Rayleigh or elastic scattering, this is a process in which a photon collides with matter without any net transfer of energy, meaning that the resulting photon retains exactly the same wavelength and frequency as the incident photon (Figure 12). In this phenomenon, the photon's electromagnetic wave causes an electron to oscillate, which then re-emits that energy in a slightly different direction, causing a change in trajectory by a small angle without gaining or losing energy in the process. This type of interaction is characteristic of low-energy photons when they pass through materials with a high atomic number, with its effect limited exclusively to an angular deviation of the original radiation.

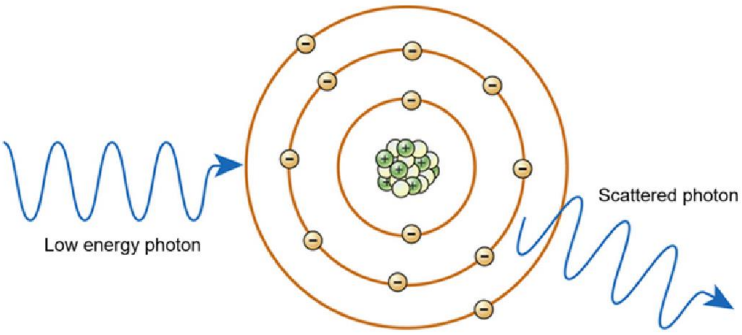

Figure 12. Coherent (elastic) photon scattering in an atom.

Photodisintegration: This is a process that occurs when high-energy γ rays, exceeding 10 MeV, interact directly with the nucleus of an atom, causing it to become excited and subsequently decay immediately into two or more daughter nuclei (Figure 13). As a result of this interaction, characteristic of nuclear fission or the splitting of the atomic nucleus, particles such as neutrons or protons are emitted, thereby releasing the energy accumulated during the impact [17].

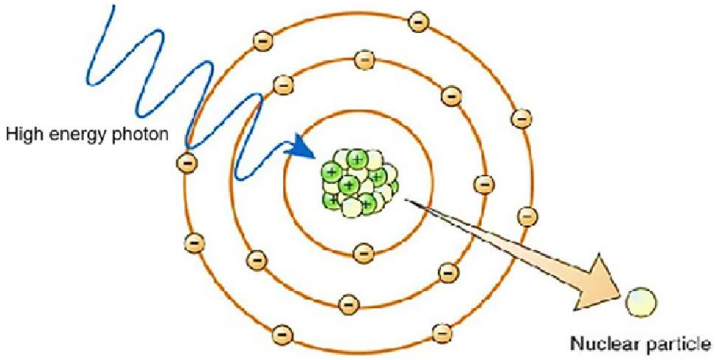

Figure 13. Photodecomposition induced by high-energy radiation.

Results and discussion

Graphs were plotted for the non-irradiated sample and the samples irradiated with gamma rays and electrons in order to observe how the samples behaved when exposed to these types of radiation. The behavior of the samples in Figure 14 shows

an overlap between the non-irradiated sample and the gamma-irradiated sample; similarly, Figure 15 shows the electron-irradiated sample.

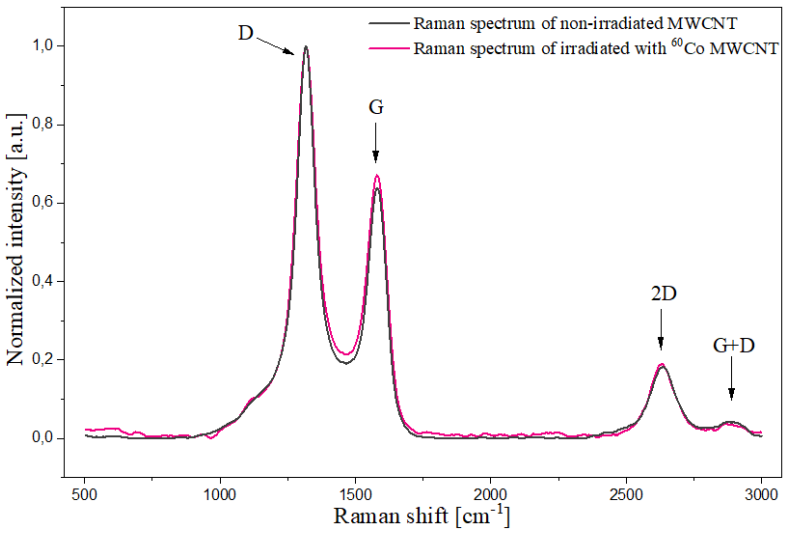

Figure 14. Comparative Raman spectra MWCNT before and after irradiation with ^{60}Co and the characteristic identification of each peak.

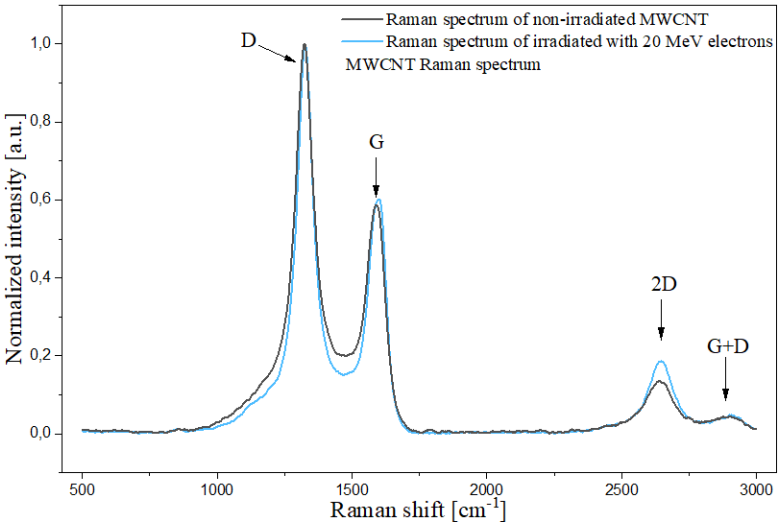

Figure 15. Comparative MWCNT Raman spectra before and after irradiation with 20 MeV electrons and the characteristic identification of each peak.

In the comparison of the Raman spectra (Figures 14 and 15), the characteristic bands of MWCNTs are clearly identified: the D band, associated with structural disorder and defects; the G band, representative of in-plane vibrations of sp^2-hybridized carbon atoms; and the 2D and G+D bands.

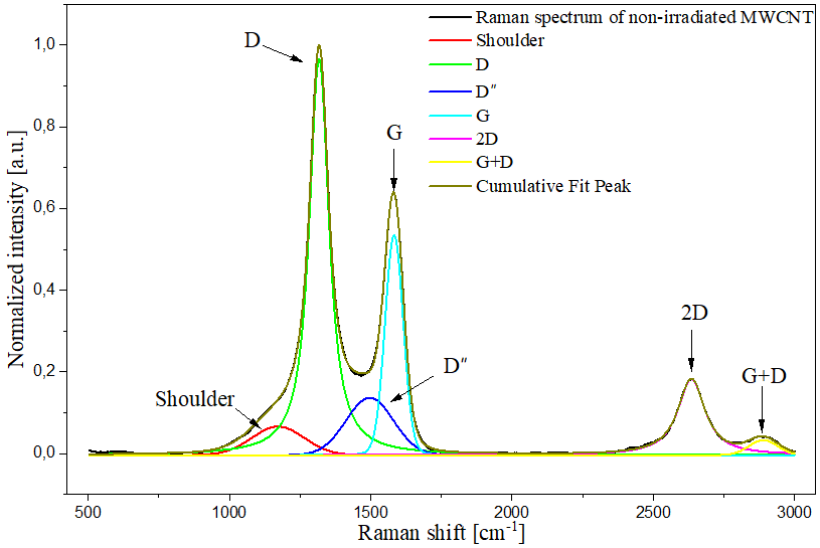

Figure 16a. Deconvolution of the pristine MWCNT sample Raman spectrum.

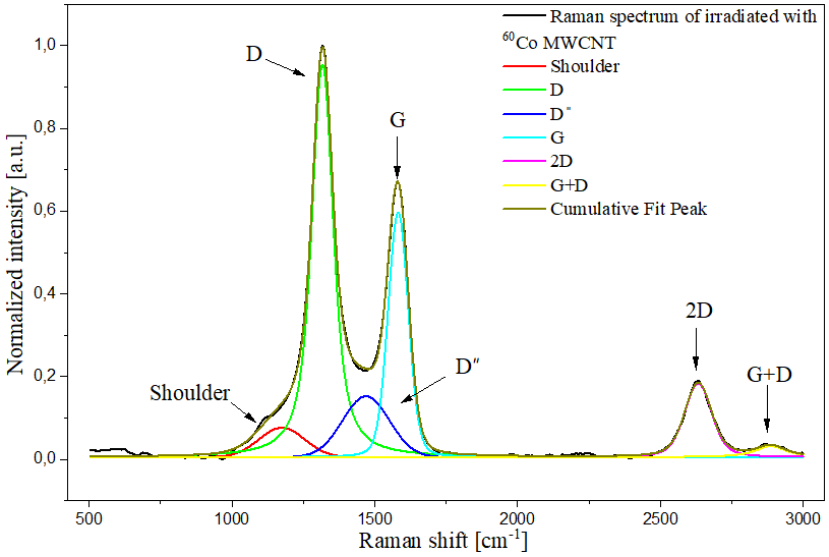

Figure 16b. Deconvolution of the irradiated with ^{60}Co gamma rays MWCNT Raman spectrum.

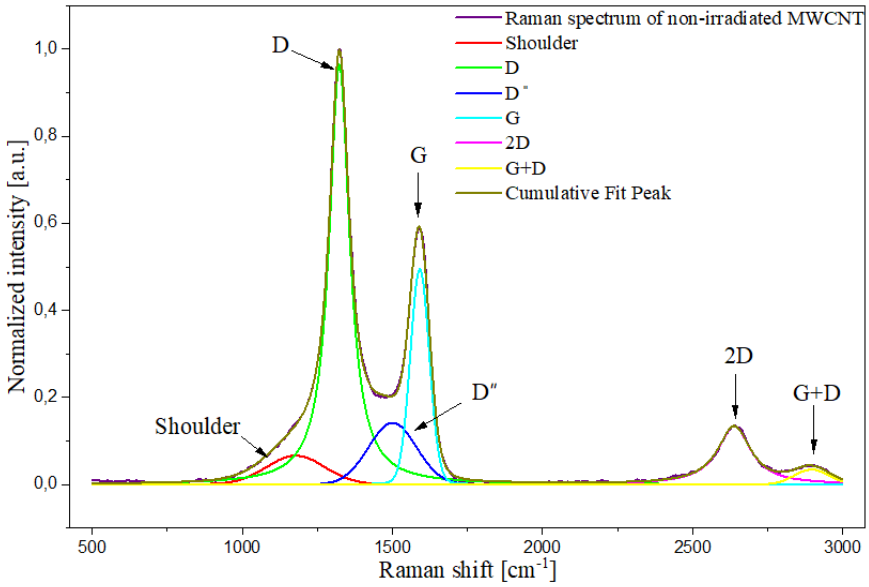

Figure 17a. Deconvolution of the pristine MWCNT sample Raman spectrum.

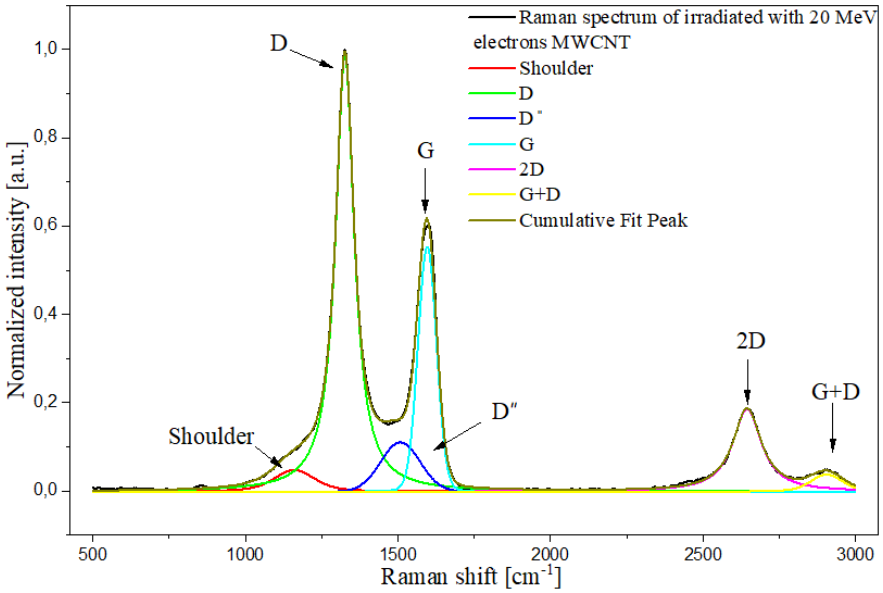

Figure 17b. Deconvolution of the irradiated with 20 MeV electrons MWCNT Raman spectrum.

Table 2 presents the statistical parameters of the reduced chi-square and the coefficient of determination, in order to achieve better peak resolution; in the irradiated or pristine samples (gamma or electrons), it is observed that in the case of R^2, all values are above 0.99 or 99%, indicating that the loss of information between the

separating bands is minimal and does not introduce any significant change in the results, and the reduced Chi-square values remain low.

Table 2. Statistical parameters of the fits made in the deconvolution process.

MWCNT	Gamma irradiation		Electron irradiation	
	Pristine sample	Irradiated sample	Pristine sample	Irradiated sample
Reduced Chi-sqr (χ^2)	6,84884E-6	2,82904E-5	1,13359E-5	1,74606E-5
R-sqr (R^2)	0.9978	0.99917	0.99961	0.99934

The data presented in Table 3 show that the band centers remained virtually unchanged following exposure to gamma and electron radiation. The absence of a substantial shift confirms the dimensional stability of the graphene lattice in MWCNTs, ruling out significant expansion or structural distortion in the material's hexagonal lattice.

Table 3. Raman shifts of the analyzed spectra main modes.

Raman shift [cm^{-1}]	Gamma irradiation		Electron irradiation	
	Pristine sample	Irradiated sample	Pristine sample	Irradiated sample
D mode	1317,59591	1317,02272	1323,45263	1326,18501
G mode	1582,91569	1582,01132	1591,22642	1596,02353
D^{II} mode	1496,66302	1469,27274	1500,46965	1508,05152
G^{I} mode	2634,71833	2631,88039	2638,10919	2644,05057
D+G mode	2889,37463	2885,62896	2896,4822	2904,80131

According to the data presented in Table 4, the samples subjected to gamma irradiation exhibit an increase in the FWHM of the D and G bands compared to the pristine sample. This broadening suggests that gamma radiation introduces defects uniformly into the lattice, leading to greater structural disorder. In contrast, electron irradiation shows the opposite behavior: the FWHM values decrease in the D and G bands after treatment. This reduction indicates that the material achieved greater

vibrational homogeneity, which is reinforced by the notable decrease in the width of the D'' mode, a parameter closely linked to the presence of disorder in the structure.

Table 4. Full Width at Half Maximum of the analyzed spectra main modes.

FWHM [cm^{-1}]	Gamma irradiation		Electron irradiation	
	Pristine sample	Irradiated sample	Pristine sample	Irradiated sample
D mode	83,21556	89,84092	81,86523	74,23969
G mode	75,92373	83,33209	74,33921	71,35861
D^{II} mode	196,78522	192,57677	187,55941	151,89855
G^{I} mode	115,72026	112,1911	134,00279	113,31219
D+G mode	119,2270	126,25866	134,63833	123,53759

Analysis of the samples using Raman spectroscopy, as shown in Figures 16a, 16b, 17a and 17b, reveals the consistent presence of the fundamental bands D, G, D'' 2D (G'), and D+G, as well as a characteristic signal known as the “low-frequency shoulder.” This spectral profile is maintained in both the reference samples and those subjected to gamma and electron irradiation.

Regarding the behavior of the D band (~1350 cm^{-1}), a contrasting phenomenon is observed depending on the type of radiation applied. In the case of gamma irradiation, Table 5 shows a decrease in its intensity compared to the original (pristine) sample.

Table 5. Intensities of the analyzed spectra main modes.

Intensity [a.u.]	Gamma irradiation		Electron irradiation	
	Pristine sample	Irradiated sample	Pristine sample	Irradiated sample
D mode	0,9695	0,9521	0,9648	0,9958
G mode	0,5342	0,5958	0,4941	0,5525
D^{II} mode	0,1363	0,1520	0,1412	0,1098
G^{I} mode	0,1831	0,1848	0,1343	0,1863
D+G mode	0,0325	0,0355	0,0341	0,0366
ID/IG	1,8149	1,5980	1,9526	1,8024

Since this band is intrinsically linked to defects and disorder in the sp^2-hybridized carbon lattice, its reduction suggests that this type of energy did not generate additional disorder but may have contributed to a stabilization of the structure. In contrast, electron irradiation caused an increase in the intensity of the D band, confirming an increase in structural disorder and defect density due to the direct impact of the particles on the nanotubes' crystal lattice.

As for the G band (~1580 cm^{-1}), both irradiation methods resulted in an increase in its intensity, reflecting a more robust response from the graphitic domains. Similarly, the 2D mode (G') also showed a significant increase in both irradiated samples. This behavior is interpreted as an improvement in long-range crystallinity or effective exfoliation of the material's concentric layers, with this phenomenon being notably more pronounced in the samples subjected to high-energy electrons. The D+G combination band experienced a slight increase in both cases, which is consistent with the presence of complex phononic interactions activated by the material's new configuration following treatment.

Finally, analysis of the intensity ratio ID/IG reveals a highly positive trend for material quality, as a clear decrease in this value is observed for both types of irradiation. This decrease is a reliable indicator that the samples have achieved a state of greater purity or better overall structural organization following the process. Regarding the "low-frequency shoulder" detected near 1200 cm^{-1}, its origin is attributed to a double resonance process.

The precise identification of these signals—particularly the D'' band and the low-frequency shoulder—was made possible by a process of spectral deconvolution using the Voight function. This technique allowed us to separate and quantify vibrational modes that often overlap or are not evident upon initial visual inspection.

Conclusions

Characterization of MWCNTs using Raman spectroscopy allowed us to identify the fundamental vibrational modes D, G, 2D (or G'), and the D+G combination band. A very important aspect of the data analysis was the spectral deconvolution process using the Voigt function; its application helped us resolve low-intensity components

that are often overlapped, making it possible to determine the presence of the “low-frequency shoulder” and the D'' band.

Regarding the stability of the crystal lattice, analysis of the central frequencies of the peaks revealed that there is no significant variance following gamma and electron irradiation. This absence of Raman shifts confirms the dimensional stability of the hexagonal graphene lattice, ruling out macroscopic distortions or radiation-induced strain. However, the study of the full width at half maximum (FWHM) provided information on local order: while gamma radiation caused a slight broadening of the D and G bands, electron irradiation resulted in narrower profiles, suggesting greater vibrational homogeneity and a reordering of the lattice.

Finally, the behavior of the D band under gamma irradiation led to a reduction in pre-existing defects (a decrease in intensity in this band), whereas electron irradiation increased the defect density. Despite these differences, both gamma and electron irradiation produced an improvement in structural quality compared to the pristine sample. This phenomenon is validated by the ID/IG intensity ratio, whose decrease under both irradiation conditions indicates greater graphitic organization and purification of the solid phase, optimizing the molecular structure of the MWCNTs.

Acknowledgements

I would like to express my gratitude to the Joint Institute for Nuclear Research, particularly its International Remote Student Training (INTERST) initiative, for giving me the opportunity to participate in this research. I also thank Dr. Antonio Leyva Fabelo for allowing me to nurture my scientific curiosity through this project, for his willingness to guide, support, and assist me throughout this brief yet enriching period, during which I was able to strengthen my academic knowledge and continue to be inspired by science.

References

1. Bumbrah GS, Sharma RM. Raman spectroscopy – basic principle, instrumentation and selected applications for the characterization of drugs of

abuse. Egypt J Forensic Sci. 2016;6(3):209–215. DOI: 10.1016/j.ejfs.2015.06.001.

2. Domingo C. Raman spectroscopy techniques applied to conservation 2011. Available at: https://digital.csic.es/handle/10261/37030
3. Santoro G, Domingo C. Raman spectroscopy of carbon nanotubes. 2007 Jan 1;40(2):175–186. Available from: http://hdl.handle.net/10261/4146
4. Castro Ramos J. Raman spectroscopy and its applications. Opt Pura Apl. 1 marzo de 2013;46(1):83-95. DOI:10.7149/OPA.46.1.83
5. Otero, Javier & Cano, Vanessa. (2015). Raman Spectroscopy: Fundamentals and Applications. DOI: 10.13140/RG.2.1.5015.5362
6. Orlando A, Franceschini F, Muscas C, Pidkova S, Bartoli M, Rovere M, et al. A Comprehensive Review of Raman Spectroscopy Applications. Chemosensors. September 13, 2021;9(9):262. DOI: 10.3390/chemosensors9090262
7. Orlando A, Franceschini F, Muscas C, Pidkova S, Bartoli M, Rovere M, et al. A Comprehensive Review on Raman Spectroscopy Applications. Chemosensors. 2021 Sep 13;9(9):262. DOI:10.3390/chemosensors9090262
8. Hodkiewicz, J. Characterizing Carbon Materials with Raman Spectroscopy. Madison, WI: Thermo Fisher Scientific; 2010. Available from: https://icpms.cz/labrulez-bucket-strapi-h3hsga3/D19504_cc33b312f3.pdf
9. Ferraro JR, Nakamoto K, Brown CW. Introductory Raman spectroscopy. 2nd ed. Amsterdam Boston: Academic Press; 2003.
10. Orlando A, Franceschini F, Muscas C, Pidkova S, Bartoli M, Rovere M, et al. A Comprehensive Review on Raman Spectroscopy Applications. Chemosensors. 2021 Sep 13;9(9):262. DOI:10.3390/chemosensors9090262
11. Bîru EI, Iovu H. Graphene Nanocomposites Studied by Raman Spectroscopy. In: Nascimento GMD, editor. Raman Spectroscopy.InTech; 2018. DOI:10.5772/intechopen.73487
12. Delgado JL, Herranz MÁ, Martín N. Carbon nanostructures: a new scientific challenge. An Quim. 2007;103(4):5-13
13. Ando Y, Zhao X, Shimoyama H, Sakai G, Kaneto K. Physical properties of multiwalled carbon nanotubes. International Journal of Inorganic Materials. 1999 Apr;1(1):77–82. DOI:10.1016/S1463-0176(99)00012-5

14. Costa S, Borowiak-Palen E, Kruszyńska M, Bachmatiuk A, Kaleńczuk RJ. Characterization of carbon nanotubes by Raman spectroscopy. Mater Sci-Pol. 2008;26(2):433-41.
15. Bîru EI, Iovu H. Graphene Nanocomposites Studied by Raman Spectroscopy. In: Nascimento GMD, editor. Raman Spectroscopy. InTech; 2018 DOI: 10.5772/intechopen.73487
16. OriginPro, Version 9.0. Northampton (MA): OriginLab Corporation; 2013. Available from: https://www.originlab.com.
17. Maqbool M. Interaction of Gamma Rays and X-Rays with Matter. In: Maqbool M, editor. An Introduction to Medical Physics. Cham: Springer International Publishing; 2017. p. 43–61. (Biological and Medical Physics, Biomedical Engineering). DOI: 10.1007/978-3-319-61540-0_3
18. Murray RL, Holbert KE. Radiation and Materials. In: Nuclear Energy. Elsevier; 2020. p. 81–99. DOI:10.1016/B978-0-12-812881-7.00005-8